

# Temporal and spectral gamma-ray properties of Mkn 421 above 250 GeV from CAT observations between 1996 and 2000

F. Piron<sup>3,\*</sup>, A. Djannati-Atai<sup>6</sup>, M. Punch<sup>6</sup>, J.-P. Tavernet<sup>4</sup>, A. Barrau<sup>4, \*\*</sup>, R. Bazer-Bachi<sup>1</sup>, L.-M. Chouquet<sup>3</sup>, G. Debiais<sup>2</sup>, B. Degrange<sup>3</sup>, J.-P. Dezelay<sup>1</sup>, P. Espigat<sup>6</sup>, B. Fabre<sup>2</sup>, P. Fleury<sup>3</sup>, G. Fontaine<sup>3</sup>, P. Goret<sup>7</sup>, C. Gouiffes<sup>7</sup>, B. Khelifi<sup>6</sup>, I. Malet<sup>1</sup>, C. Masterson<sup>6</sup>, G. Mohanty<sup>3,\*\*\*</sup>, E. Nuss<sup>2,\*</sup>, C. Renault<sup>4, \*\*</sup>, M. Rivoal<sup>4</sup>, L. Rob<sup>5</sup>, and S. Vorobiov<sup>3</sup>

<sup>1</sup> Centre d'Etudes Spatiales des Rayonnements, Université Paul Sabatier, Toulouse, France (INSU/CNRS)

<sup>2</sup> Groupe de Physique Fondamentale, Université de Perpignan, France

<sup>3</sup> Laboratoire de Physique Nucléaire des Hautes Energies, Ecole Polytechnique, Palaiseau, France (IN2P3/CNRS)

<sup>4</sup> Laboratoire de Physique Nucléaire et de Hautes Energies, Universités Paris VI/VII, France (IN2P3/CNRS)

<sup>5</sup> Nuclear Center, Charles University, Prague, Czech Republic

<sup>6</sup> Physique Corpusculaire et Cosmologie, Collège de France et Université Paris VII, France (IN2P3/CNRS)

<sup>7</sup> Service d'Astrophysique, Centre d'Etudes de Saclay, France (CEA/DSM/DAPNIA)

Received 10 April 2001 / Accepted 6 June 2001

**Abstract.** The  $\gamma$ -ray emission above 250 GeV from the BL Lac object Markarian 421 was observed by the CAT Cherenkov imaging telescope between December, 1996, and June, 2000. In 1998, the source produced a series of small flares, making it the second extragalactic source detected by CAT. The time-averaged differential spectrum has been measured from 0.3 to 5 TeV, which is well fitted with a power law:  $\frac{d\phi}{dE} \propto E_{\text{TeV}}^{-2.88 \pm 0.12^{\text{stat}} \pm 0.06^{\text{syst}}}$ . In 2000, the source showed an unprecedented activity, with variability time-scales as short as one hour, as for instance observed during the night between 4 and 5 February. The 2000 time-averaged spectrum measured is compatible with that of 1998, but some indication of a spectral curvature is found between 0.3 and 5 TeV. The possibility of TeV spectral hardening during flares is also discussed, and the results are compared to those obtained on the other TeV BL Lac, Markarian 501.

**Key words.** Galaxies: active – Galaxies: nuclei – BL Lacertæ objects: individual: Mkn 421 – Gamma-rays: observations

## 1. Introduction

Among Active Galactic Nuclei (AGNs), blazars are those radio-loud objects having a jet pointing towards the observer, which has a relatively high bulk Lorentz factor, giving rise to a strong Doppler boosting of the observed fluxes. Blazar emission is dominated by their jet power output, which is mainly non-thermal, extending over more than fifteen energy decades. At low energies, their featureless optical continuum as well as their strong radio and optical polarization are due to synchrotron radiation of the magnetized plasma jet. At high energies, blazar jets also show remarkable properties. During the last ten years, the EGRET detector, operating above 30 MeV on board the Compton Gamma-Ray Observatory,

definitively opened the field of high-energy astrophysics by revealing that most extragalactic strong  $\gamma$ -ray emitters were blazars (von Montigny et al. 1995; Hartman et al. 1999). Their  $\gamma$ -radiation power often dominates their entire spectrum, and it must be produced in a small enough region to account for rapid variability, already observed on time-scales less than one hour at TeV energies (Gaidos et al. 1996). Although the origin of jets is still uncertain, the study of their  $\gamma$ -ray emission in blazars can shed light on the nature and content of their plasma ( $e^+e^-$  pairs or  $e^-p$ ), and give new insight into the high-energy particle acceleration and cooling processes occurring at the sub-parsec scale. Ultimately this could give useful information on how jets take form and lead to a better understanding of the energy extraction mechanisms in the surroundings of the central supermassive black hole.

Send offprint requests to: F. Piron, e-mail: piron@in2p3.fr

\* Present address: GAM, CC 085 - Bât. 11, Univ. de Montpellier II, Place Eugène Bataillon, 34095 Montpellier Cedex 5, France

\*\* Present address: Institut des Sciences Nucléaires, 53 avenue des Martyrs, 38026 Grenoble Cedex, France

\*\*\* Present address: IGPP, University of California, Riverside, CA 92521, USA

Markarian 421 (Mkn 421) is the closest known BL Lac blazar (at a redshift of 0.031), and the first discovered in the high and very-high energy (VHE) ranges. It was first detected as a weak source by the EGRET instrument up to a few GeV during summer 1991 (Lin et al. 1992). Eight months later, the

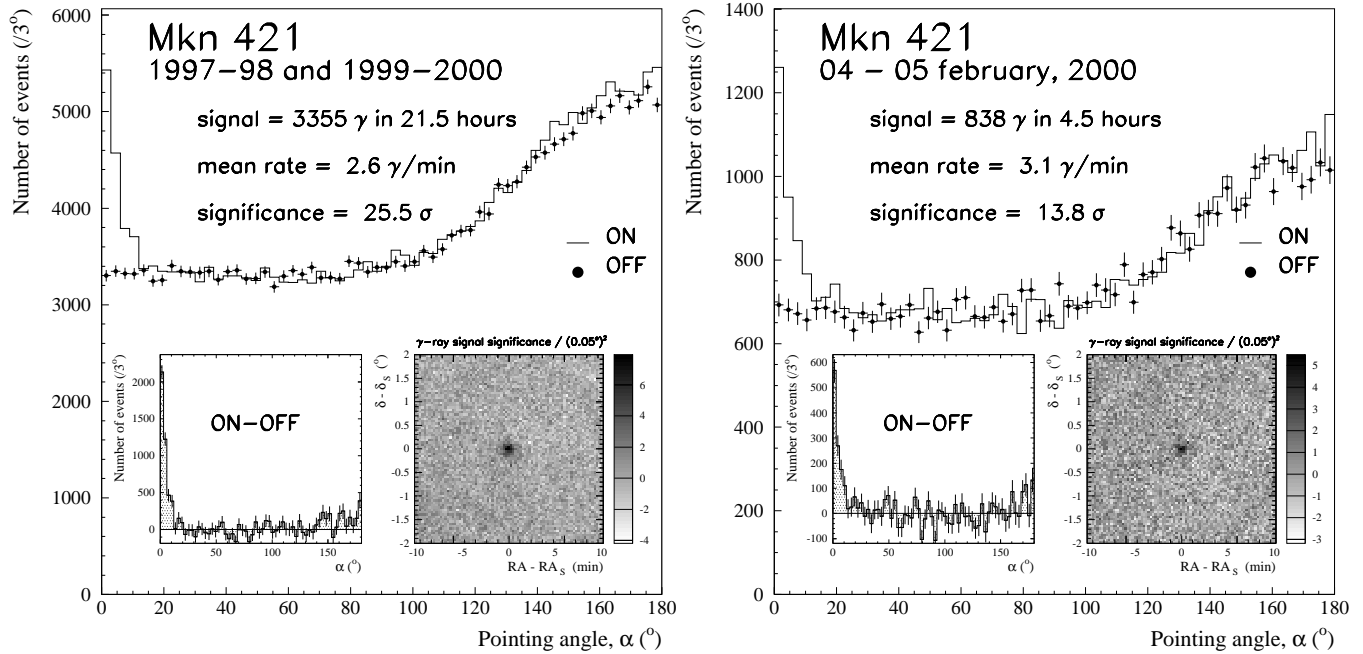


**Fig. 1.** The Mkn 421  $\gamma$ -ray signal seen with the CAT imaging telescope, for the most significant observations (signal significance greater than  $3\sigma$  in  $\sim 30$  min) taken in 1997–98 and 1999–2000 at zenith angle  $\theta_z < 45^\circ$  (left panel), and for the highest flare, recorded between 4 and 5 February, 2000 (right panel). In each panel, the main plot shows the pointing angle,  $\alpha$ , distribution for ON (solid line) and OFF data (points with error bars, same duration as ON data), and the bottom-left inset gives the “ON–OFF” distribution; events are selected by the  $Q_4$ ,  $Q_{\text{tot}}$ , and  $\mathcal{P}(\chi^2)$  cuts (see text), and the values quoted in legend come from the additional cut  $\alpha < 6^\circ$  (first two bins). The bottom-right inset shows the significance map of event excess per bin of  $0.05^\circ$ , obtained from the “ON–OFF” distribution of reconstructed angular origins (no cut on  $\alpha$ ): the source lies at the centre, and the axes denote the relative right ascension and declination with respect to the source coordinates ( $RA_S$  and  $\delta_S$ ).

Whipple Observatory detected a clear signal from this object between 0.5 and 1.5 TeV (Punch et al. 1992). Since then, Mkn 421 has been confirmed many times as a VHE source by various atmospheric Cherenkov imaging telescopes, e.g. again by the Whipple Observatory (Krennrich et al. 1997), by the stereoscopic system of HEGRA (Petry et al. 1996) and by the CAT (Cherenkov Array at Thémis) experiment (Piron et al. 1998, 1999b). Along with Markarian 501 (Mkn 501), Mkn 421 has thus become one of the two extragalactic sources of the Northern hemisphere which has been firmly established in the VHE range. It has been also one of the most studied blazars and the target of several multi-wavelength observation campaigns from the radio band to the  $\gamma$ -ray range (see, e.g., Macomb et al. 1995; Buckley et al. 1996; Takahashi et al. 1996; Takahashi et al. 1999, 2000; Charlot et al. 1998; Maraschi et al. 1999). Recently, a major step was achieved during the 1999–2000 winter by the CELESTE atmospheric Cherenkov sampling experiment, which detected Mkn 421 for the first time around 50 GeV, filling the last energy gap still remaining on this source between satellites and ground-based detectors. These observations, made in part simultaneously with the CAT telescope, have been presented by Holder et al. (2001).

In this paper we concentrate on the temporal variability and the spectral properties of Mkn 421 above 250 GeV, as seen by the CAT experiment since it began operation in autumn 1996. Sect. 2 describes the detector and the analysis methods used to extract the signal and the spectra. The Mkn 421 data sample, the light curves up to June 2000 and the corresponding spectra are presented in Sect. 3. We discuss our results in Sect. 4, comparing them with those from other ground-based atmospheric Cherenkov telescopes, and with those obtained on Mkn 501. The conclusions are given in Sect. 5.

## 2. Experimental setup and data analysis

### 2.1. Telescope characteristics

Located on the site of the former solar plant at Thémis in the French Pyrénées ( $2^\circ$  East,  $42^\circ$  North, altitude 1650 m above sea level), the CAT telescope (Barrau et al. 1998) uses the Cherenkov imaging technique. Its  $17.8 \text{ m}^2$  mirror collects the Cherenkov light emitted by the secondary particles produced during the development of atmospheric showers and forms their image in its focal plane. The CAT camera has a full field of view of  $4.8^\circ$  but the present study is limited to the  $3.1^\circ$  fine-grained inner part, which is comprised of 546 phototubes with  $0.12^\circ$  angular diameter, arranged in an hexagonal matrix. This very high definition, combined with fast electronics whose

integration time (12 ns) matches the Cherenkov flash's short duration, is an efficient solution of the two main problems of night-sky and cosmic-ray backgrounds which confront such  $\gamma$ -ray detectors. Firstly, the detection threshold, which is determined by the night-sky noise, is as low as 250 GeV at Zenith<sup>1</sup>. Secondly, the capability of rejecting the huge cosmic-ray background (protons, nuclei) is improved by an accurate analysis based on the comparison of individual images with theoretical mean  $\gamma$ -ray images. This method, very briefly reviewed in Sect. 2.2, is specific to the CAT experiment and has been described in detail in Le Bohec et al. (1998).

## 2.2. Gamma-ray signal extraction

In order to improve the hadronic rejection and stabilize the background level near the detection threshold, and to compensate for possible slight changes in the detector response between different epochs of observation, we eliminate the noisiest pixels and require the fourth-brightest-pixel's charge in the image  $Q_4 > 3$  p.e. (photo-electrons) and the image's total charge  $Q_{\text{tot}} > 30$  p.e.

An efficient discrimination between  $\gamma$  and hadron-induced showers is then achieved by looking at the shape and the orientation of the images. Since  $\gamma$ -ray images are rather thin and ellipsoidal while hadronic images are more irregular, a first cut is applied which selects images with a “ $\gamma$ -like” shape; it is based on a  $\chi^2$  fit to a mean light distribution predicted from electromagnetic showers, and a probability  $\mathcal{P}(\chi^2) > 0.35$  is required. In addition, since  $\gamma$ -ray images are expected to point towards the source angular position in the focal plane whereas cosmic-ray directions are isotropic, a second cut  $\alpha < 6^\circ$  is used in the case of a point-like source, where the pointing angle  $\alpha$  is defined as the angle at the image barycentre between the actual source angular position and the source position as reconstructed by the fit. As a result, this procedure rejects 99.5% of hadronic events while keeping 40% of  $\gamma$ -ray events; the Crab nebula, which is generally considered as the standard candle for VHE  $\gamma$ -ray astronomy, is detected at a  $4.5\sigma$  level in one hour.

Fig. 1 shows the  $\alpha$  distributions obtained from two data samples taken on Mkn 421, for ON and OFF-source observations (the latter being taken at the same telescope elevation in order to monitor the hadronic background), and the corresponding distributions for  $\gamma$ -rays obtained by “ON–OFF” subtraction (bottom-left insets). The signal is clearly seen in the direction of the source (small  $\alpha$ ), though the direction of some  $\gamma$ -rays is mis-identified, giving a small signal at  $\alpha \sim 180^\circ$ . As stated above, the  $\chi^2$  fit also allows the angular origin of  $\gamma$ -ray events to be determined with good accuracy as it uses the information contained in the images' asymmetrical longitudinal light profile. In Fig. 1, the bottom-right insets show the signifi-

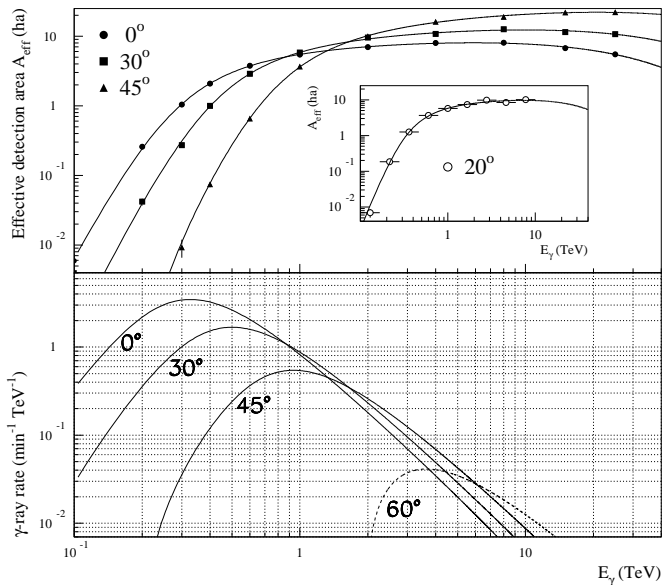


**Fig. 2.** CAT effective detection area (top) and differential trigger rate (bottom) for  $\gamma$ -ray showers after event selection.

Top: each point in the main panel is a simulation, while full lines come from an analytical 2D-formula  $\mathcal{A}_{\text{eff}}(\theta_z, E_{\gamma})$  allowing interpolation over zenith angle and energy. The inset compares the prediction of this interpolation for  $\theta_z=20^\circ$  with an independent simulation (open circles);  
Bottom: differential  $\gamma$ -ray trigger rate ( $\frac{d\phi}{dE} \times \mathcal{A}_{\text{eff}}$ ), for a typical spectrum  $\frac{d\phi}{dE} = 3.0 E_{\text{TeV}}^{-2.55} \times 10^{-11} \text{ cm}^{-2} \text{ s}^{-1} \text{ TeV}^{-1}$  and different values of  $\theta_z$ . The dashed curve at  $60^\circ$  is only indicative, as the interpolation  $\mathcal{A}_{\text{eff}}$  must be still validated for large zenith angles ( $\theta_z \gtrsim 45^\circ$ ).

cance map of  $\gamma$ -ray event excesses: the angular resolution *per event* is  $0.11^\circ$  (i.e., of the order of the pixel size), allowing a bright source to be localized with an accuracy better than  $1'$  (dominated by systematics).

## 2.3. Spectral analysis

VHE  $\gamma$ -ray spectra result from particle acceleration processes and thus they are expected to steepen above a given energy; this combines with the energy resolution currently achieved by imaging Cherenkov atmospheric detectors (20% at best) to cause a considerable event flow into higher *estimated* energy intervals. Starting with an observed differential  $\gamma$ -ray trigger rate, one therefore needs a global forward-folding method, using the knowledge of the detector response ( $\gamma$ -ray effective detection area, energy resolution), *as well as a parameterization of the spectral shape*. Therefore, we have chosen a maximum likelihood method which directly provides relevant physical results for the present problem, namely the values of the most probable spectral parameters and their covariance matrix.

The image analysis described in Sect. 2.2 also yields the energy of each hypothesised  $\gamma$ -ray shower. The spectral analysis presented below involves the exact energy-resolution function  $\Upsilon$ , which is characterised by a r.m.s. of 22% (inde-

<sup>1</sup> The threshold is defined here following the usual convention for atmospheric Cherenkov detectors, i.e. as the energy at which the differential  $\gamma$ -ray rate is maximum at the trigger level for a Crab-like spectrum. As shown in Fig. 2, it is somewhat higher after the event selection applied at the analysis level.

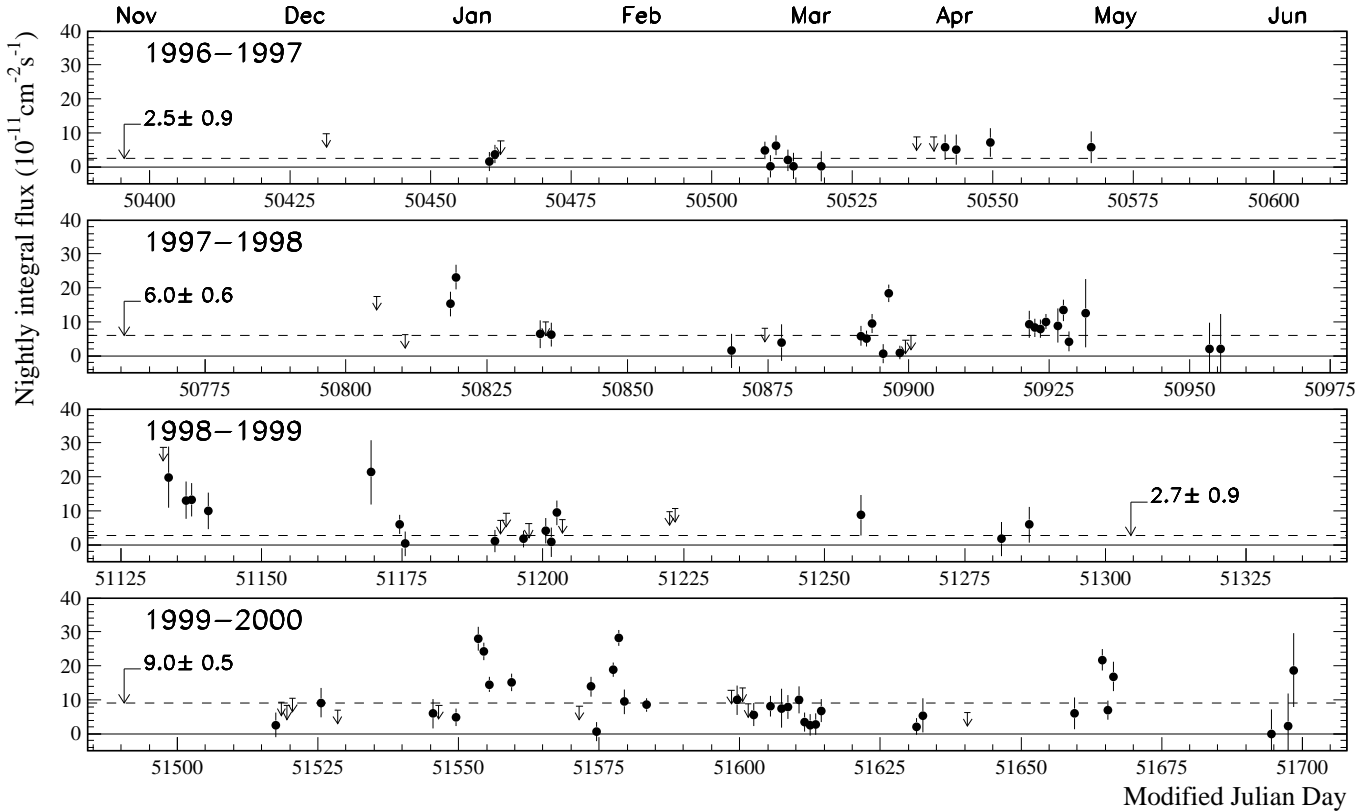


**Fig. 3.** Mkn 421 nightly-averaged integral flux above 250 GeV between December, 1996, and June, 2000. The  $\gamma$ -ray effective area has been weighted using a differential index of  $-2.9$ , in order to estimate the integral flux for observations far from the Zenith (see appendix A.2). Arrows stand for  $2\sigma$  upper-limits when no signal was recorded, and dashed lines show the mean flux for each observation year.

pendent of energy) and which includes possible bias in energy reconstruction close to the detection threshold. This function has been determined by detailed Monte-Carlo simulations of the telescope response, as has the effective detection area  $\mathcal{A}_{\text{eff}}$ , which includes the effect of event-selection efficiency (see Fig. 2). The simulations have been checked and calibrated on the basis of several observables, especially by using muon rings and the nearly-pure  $\gamma$ -ray signal from the highest flare of Mkn 501 in April 1997 (Piron et al. 1999a).

With typical statistics of  $\sim 1000$   $\gamma$ -ray events and signal-to-background ratio of  $\sim 0.4$  (as obtained on the Crab nebula), a spectrum can be determined with reasonable accuracy as follows. First we define a set  $\{\Delta_{i_z}\} \equiv \{[\theta_{i_z}^{\min}, \theta_{i_z}^{\max}]\}_{i_z=1, n_z}$  of  $n_z$  zenith angle bins, with a width (between 0.02 and 0.04 in cosine) small enough compared to the variation scale of  $\Upsilon$  and  $\mathcal{A}_{\text{eff}}$ ;  $\Delta_1$  corresponds to the transit of the source at Thémis, and  $\Delta_{n_z}$  to the maximum angle fixed by the data sample. Then we define  $n_e$  estimated energy bins  $\{\Delta_{i_e}\} \equiv \{[\tilde{E}_{i_e}^{\min}, \tilde{E}_{i_e}^{\max}]\}_{i_e=1, n_e}$ , with a width ( $\geq 0.2$  in  $\log_{10} E_{\text{TeV}}$ ) at least twice as large as the typical width of the function  $\Upsilon$ . The maximum energy  $\tilde{E}_{n_e}^{\max}$  is fixed by the available statistics. Finally, we define a set of bins  $\{\Delta_{i_z, i_e}\} \equiv \{\Delta_{i_z} \otimes \Delta_{i_e}\}_{i_z=1, n_z; i_e=i_{e1}(i_z), n_e}$ ; for each  $\Delta_{i_z}$  bin, the lowest energy

(and thus the bin  $\Delta_{i_{e1}(i_z)}$ ) is determined by the telescope detection threshold which increases with zenith angle (see Fig. 2).

Within each  $\Delta_{i_z, i_e}$  2D-bin, the number of events passing the selection cuts is determined separately for all ON and OFF-source data, and the maximum-likelihood estimation of the spectral parameters is performed following the procedure detailed in appendix A.1. The likelihood-function expression does not rely on a straightforward “ON–OFF” subtraction as in usual spectral analyses, but on the *respective* Poissonian distributions of ON and OFF events. In particular, this allows possible low statistics to be treated in a rigorous manner. No hypothesis is required on the background (OFF) shape, but two hypotheses are successively considered for the differential  $\gamma$ -ray spectrum  $\frac{d\phi}{dE}$ : *i*) a simple power law,  $\phi_0^{\text{pl}} E_{\text{TeV}}^{-\gamma^{\text{pl}}}$  (hyp.  $\mathcal{H}^{\text{pl}}$ ), which is often a good approximation, at least within a restricted energy range (over one or two orders of magnitude), and *ii*) a curved shape,  $\phi_0^{\text{cs}} E_{\text{TeV}}^{-(\gamma^{\text{cs}} + \beta^{\text{cs}} \log_{10} E_{\text{TeV}})}$  (hyp.  $\mathcal{H}^{\text{cs}}$ ). The latter parameterization, previously used by the Whipple group for the study of Mkn 421 and Mkn 501 (Krennrich et al. 1999a), corresponds to a parabolic law in a  $\log(\nu F(\nu))$  vs.  $\log(\nu)$  representation, where  $\nu F(\nu) \equiv E^2 \frac{d\phi}{dE}$  and  $E = h\nu$ .

The relevance of  $\mathcal{H}^{\text{pl}}$  with respect to  $\mathcal{H}^{\text{cs}}$  is estimated from the likelihood ratio of the two hypotheses, which is defined as

$\lambda = 2 \log \left( \frac{\mathcal{L}^{\text{cs}}}{\mathcal{L}^{\text{pl}}} \right)$ : it behaves (asymptotically) like a  $\chi^2$  with one degree of freedom and permits the search for possible spectral curvature. For each data sample, the spectral law finally retained is given by the most relevant parameterization of the differential spectrum. In the following, we chose to represent each spectrum as a function of the *true* photon energy by an area corresponding to the 68% confidence level contour given by the likelihood method.

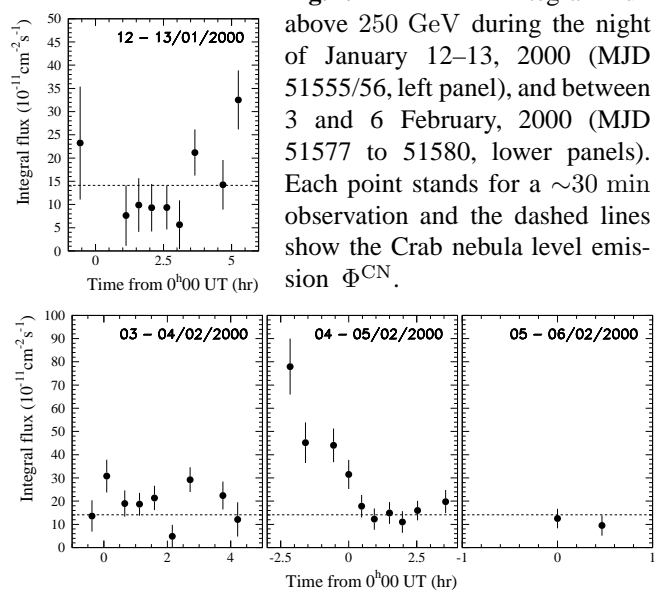
### 3. Results

#### 3.1. Data sample and light curves

The complete data sample consists of observations taken between December, 1996, and June, 2000. During these periods, the source was systematically observed in a range of zenith angle extending from close to the Zenith up to  $45^\circ$ . The intensity of the source did not influence the observation strategy. However, a selection based on criteria requiring clear moonless nights and stable detector operation has been applied: this leaves a total of 139 hours of on-source (ON) data, together with 57 hours on control (OFF) regions. The different light curves of the four observation periods are shown in Fig. 3. We used a differential index of  $-2.9$ , which is representative of all spectral measurements presented in Sect. 3.2, to estimate the integral flux above 250 GeV for all data, especially those taken far from the Zenith: this procedure is detailed in appendix A.2.

As can be seen in Fig. 3, the flux of Mkn 421 changed significantly between 1996–97 and 1997–98: almost quiet during the first period (with a mean flux  $\Phi_{>250 \text{ GeV}} = 2.5 \pm 0.9 \times 10^{-11} \text{ cm}^{-2} \text{ s}^{-1}$ ), the source showed a higher mean activity during the second period ( $\Phi_{>250 \text{ GeV}} = 6.0 \pm 0.6 \times 10^{-11} \text{ cm}^{-2} \text{ s}^{-1}$ ), with small bursts in January and March sometimes showing up in excess of the steady flux from the Crab nebula (which is  $\Phi^{\text{CN}} = 14.10 \pm 0.35 \times 10^{-11} \text{ cm}^{-2} \text{ s}^{-1}$  above 250 GeV, see Piron 2000). In 1998–99, the mean VHE emission of Mkn 421 ( $\Phi_{>250 \text{ GeV}} = 2.7 \pm 0.9 \times 10^{-11} \text{ cm}^{-2} \text{ s}^{-1}$ ) decreased to a level comparable to that of 1996–97. In spite of some activity detected during the winter, the weather conditions in Thémis caused a very sparse source coverage. Nevertheless in the beginning of 2000 Mkn 421 showed a remarkable increase in activity, exhibiting a series of huge bursts. As seen in Fig. 3, the bursts recorded in January and February 2000 clearly appear as the highest ever seen by CAT from this source in four years with a nightly-averaged integral flux culminating at  $\sim 2 \Phi^{\text{CN}}$  and a large night-to-night variability.

VHE intra-night variability was also observed on a few occasions. For instance during the night of January 12–13, the source intensity increased by a factor of 3.8 in  $\sim 2$  hours, from  $\sim 0.6 \Phi^{\text{CN}}$  to  $\sim 2.3 \Phi^{\text{CN}}$  (with a  $\chi^2$  per d.o.f of 2.5 for the absence of any variation), as can be seen in Fig. 4 (upper-left panel). At the bottom of this figure, Mkn 421 light curves are also shown for three nights from the 3<sup>rd</sup> to the 5<sup>th</sup> February. While the fluxes recorded by CAT during the first and last nights were stable, respectively  $\Phi_{>250 \text{ GeV}} \simeq 1.3 \Phi^{\text{CN}}$  (over 4 hours) and  $\Phi_{>250 \text{ GeV}} \simeq 0.7 \Phi^{\text{CN}}$  (over 1 hour), the source activity changed dramatically in a few hours during the second



night (February 4–5). The CAT telescope started observation while the source emission was at a level of  $5.5 \Phi^{\text{CN}}$ . This flux is comparable to the historically highest TeV flux ever recorded, i.e., that of Mkn 501 during the night of April 16<sup>th</sup>, 1997 (Djannati-Ataï et al. 1999). In spite of the low source elevation ( $\theta_z = 44^\circ$ ) 124  $\gamma$ -ray events with a signal significance of  $6.5 \sigma$  were detected during the first 30 minutes of observation. This may be compared to the 838  $\gamma$ -ray events and significance of  $13.8 \sigma$  obtained during the whole night (see Fig. 1). After this first episode, the source intensity was reduced by a factor of 2 in 1 hour and by a factor of 5.5 in 3 hours. In Fig. 4, each point stands for a  $\sim 30$  min observation but a finer binning in time does not show any additional interesting features, confirming that CAT started observation after the flare maximum.

#### 3.2. 1998 and 2000 time-averaged spectra

The data used in this section consist of a series of  $\sim 30$  min acquisitions for which a  $\gamma$ -ray signal with significance greater than  $3\sigma$  was recorded, and they have been further limited to zenith angles  $\theta_z < 28^\circ$ , i.e., to a configuration for which the detector calibration has been fully completed. The spectral study is thus based on 6.2 hours of on-source (ON) data taken in 1998 and 8.4 hours in 2000. Though this data selection reduces somewhat the total number of  $\gamma$ -ray events, it provides a high signal-to-noise ratio, minimizes systematic effects, and allows a robust spectral determination. Concerning systematic effects, another favourable factor is the low night-sky background in the field of view due to the lack of bright stars around the source.

Systematic errors are thus mainly due to the uncertainty on the absolute energy scale, which comes from possible variations of the atmosphere transparency and light-collection efficiencies during the observation periods. To a lesser extent, they are also due to limited Monte-Carlo statistics in the determination of the effective detection area. These errors, assumed to be the same for all spectra, are implicitly con-

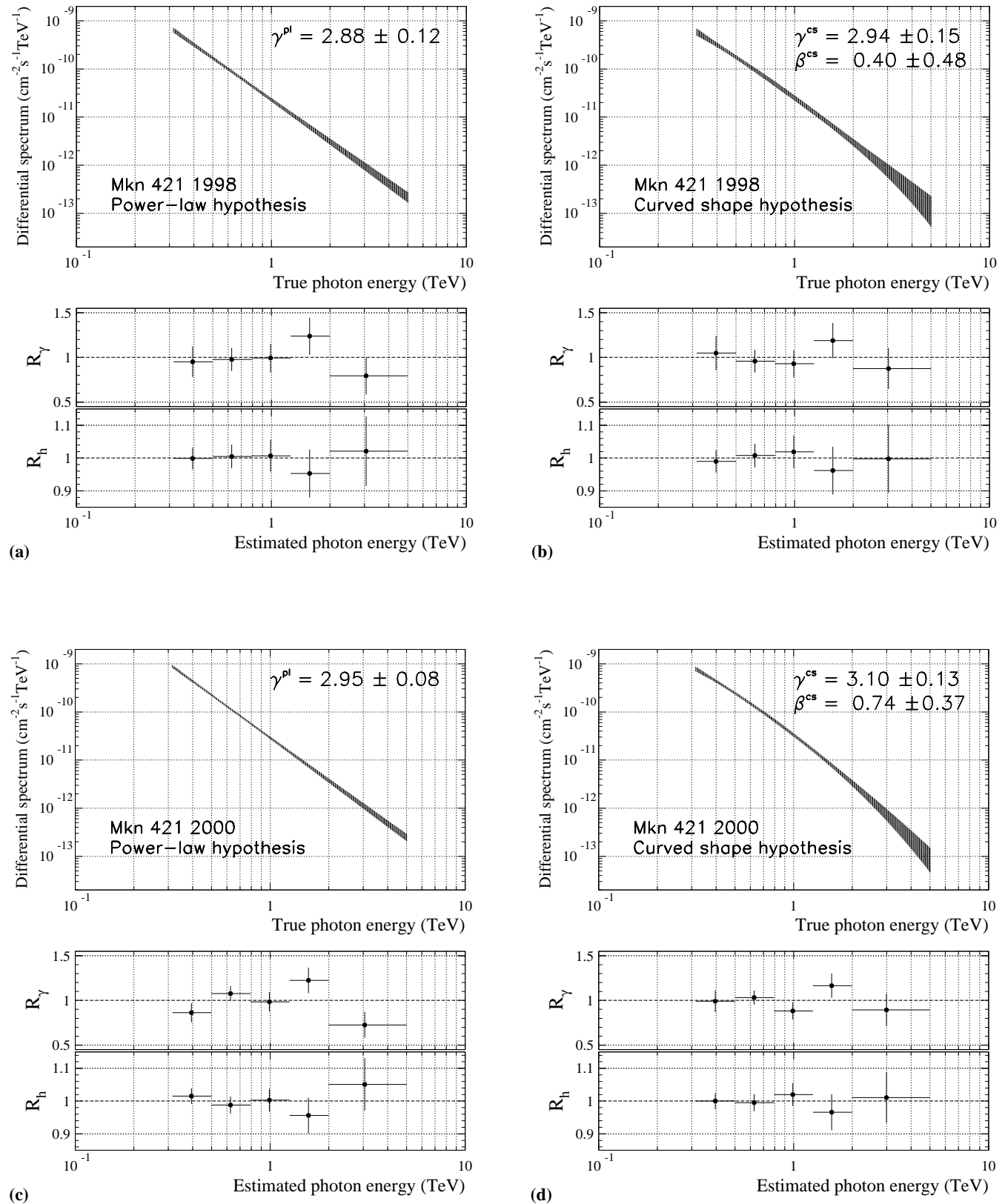


**Fig. 5.** Mkn 421 time-averaged spectra between 0.3 and 5.0 TeV in 1998 and 2000, for the power-law and curved shape hypotheses. The areas show the 68% confidence level contour given by the likelihood method. In each of the four panels, the two lower plots give the ratio, in each bin of *estimated* energy, of the predicted number of events to that which is observed both for the  $\gamma$ -ray signal ( $R_\gamma$ ) as well as for the hadronic background ( $R_h$ ).

**Table 1.** Characteristics of the Mkn 421 spectra obtained in this paper. For each spectrum we indicate the observation period, the total energy band used in the likelihood method,  $\Delta\widetilde{E}_\gamma$ , the total observed number of  $\gamma$ -ray events,  $S_\gamma$ , the spectral parameters obtained in the  $\mathcal{H}^{\text{pl}}$  and  $\mathcal{H}^{\text{cs}}$  hypotheses, and the likelihood ratio  $\lambda$ . We also quote the decorrelation energy in the  $\mathcal{H}^{\text{pl}}$  hypothesis,  $E_d$ , the energy  $E_0^{\text{cs}}$  at which the energy-dependent exponent  $\gamma_l^{\text{cs}}(E_{\text{TeV}}) = \gamma^{\text{cs}} + \beta^{\text{cs}} \log_{10} E_{\text{TeV}}$  has a minimal error in the  $\mathcal{H}^{\text{cs}}$  hypothesis (see appendix B.2), and the corresponding value  $\gamma_0^{\text{cs}} \equiv \gamma_l^{\text{cs}}(E_0^{\text{cs}})$ . The energies are given in TeV, and the flux constants are given in units of  $10^{-11} \text{ cm}^{-2} \text{ s}^{-1} \text{ TeV}^{-1}$ .

Period	$\Delta\widetilde{E}_\gamma$ (TeV)	$S_\gamma$	$\phi_0^{\text{pl}}$	$\gamma^{\text{pl}}$	$E_d$	$\phi_0^{\text{cs}}$	$\gamma^{\text{cs}}$	$\beta^{\text{cs}}$	$E_0^{\text{cs}}$	$\gamma_0^{\text{cs}}$	$\lambda$
1998	0.3–5.0	735±57	2.29±0.20	2.88±0.12	0.69	2.51±0.32	2.94±0.15	0.40±0.48	0.73	2.88±0.14	0.75
2000	0.3–5.0	1424±71	2.90±0.18	2.95±0.08	0.63	3.34±0.28	3.10±0.13	0.74±0.37	0.61	2.94±0.10	4.90
4–5/02/2000	0.3–2.0	609±40	3.16±0.34	2.82±0.15	0.57	3.25±0.37	3.08±0.39	0.63±0.81	0.37	2.81±0.17	0.61

sidered in the following and they have been estimated from detailed simulations (Piron 2000):  $(\Delta\phi_0/\phi_0)^{\text{syst}} = \pm 20\%$ ,  $(\Delta\gamma)^{\text{syst}} = \pm 0.06$ , and  $(\Delta\beta)^{\text{syst}} = \pm 0.03$ .

The 1998 and 2000 time-averaged spectra are shown in Fig. 5, both in the power-law and curved shape hypotheses. The statistics used for their extraction are detailed in appendix B.1, the spectral parameters are summarized in Table 1, and their covariance matrices are given in appendix B.2. In each panel of Fig. 5, the two lower plots give the ratio, in each bin of *estimated* energy, of the predicted number of events to that which is observed both for the  $\gamma$ -ray signal ( $R_\gamma$ ) as well as for the hadronic background ( $R_h$ ). This is another means to check the validity of the parameters estimation, and to compare between the two hypotheses on the spectral shape.

As can be seen in Fig. 5a, the power law accounts very well for the 1998 time-averaged spectrum. The likelihood ratio value is low ( $\lambda=0.75$ , corresponding to a chance probability of 0.39), and the curvature term is compatible with zero ( $\beta^{\text{cs}}=0.40\pm0.48^{\text{stat}}$ ). Thus, we find the following differential spectrum:

$$\frac{d\phi}{dE} = (2.29 \pm 0.20^{\text{stat}} \pm 0.46^{\text{syst}}) 10^{-11} \text{ cm}^{-2} \text{ s}^{-1} \text{ TeV}^{-1} \times E_{\text{TeV}}^{-2.88 \pm 0.12^{\text{stat}} \pm 0.06^{\text{syst}}}.$$

On the contrary, Fig. 5d shows some evidence for a curvature in the 2000 time-averaged spectrum, with a relatively high likelihood ratio value ( $\lambda=4.90$ , corresponding to a chance probability of 0.027). The lower plots of Fig. 5d, when compared to those of Fig. 5c, directly confirm that a curved spectrum provides a better fit to the data. This curvature is equivalent to an energy-dependent exponent  $\gamma_l^{\text{cs}}(E_{\text{TeV}}) = \gamma^{\text{cs}} + \beta^{\text{cs}} \log_{10} E_{\text{TeV}}$ . Table 1 shows the energy  $E_0^{\text{cs}}$  at which the error on  $\gamma_l^{\text{cs}}(E_{\text{TeV}})$  is minimal, as well as the corresponding value  $\gamma_0^{\text{cs}} \equiv \gamma_l^{\text{cs}}(E_0^{\text{cs}})$ ; the latter value is in all cases very close to that of  $\gamma^{\text{pl}}$  (in the absence of curvature), showing the consistency of the spectral analysis. Thus, we finally retain the following parameterization for the 2000 period:

$$\frac{d\phi}{dE} = (3.34 \pm 0.28^{\text{stat}} \pm 0.67^{\text{syst}}) 10^{-11} \text{ cm}^{-2} \text{ s}^{-1} \text{ TeV}^{-1} \times E_{\text{TeV}}^{-3.10 \pm 0.13^{\text{stat}} \pm 0.06^{\text{syst}} - (0.74 \pm 0.37^{\text{stat}} \pm 0.03^{\text{syst}}) \log_{10} E_{\text{TeV}}}.$$

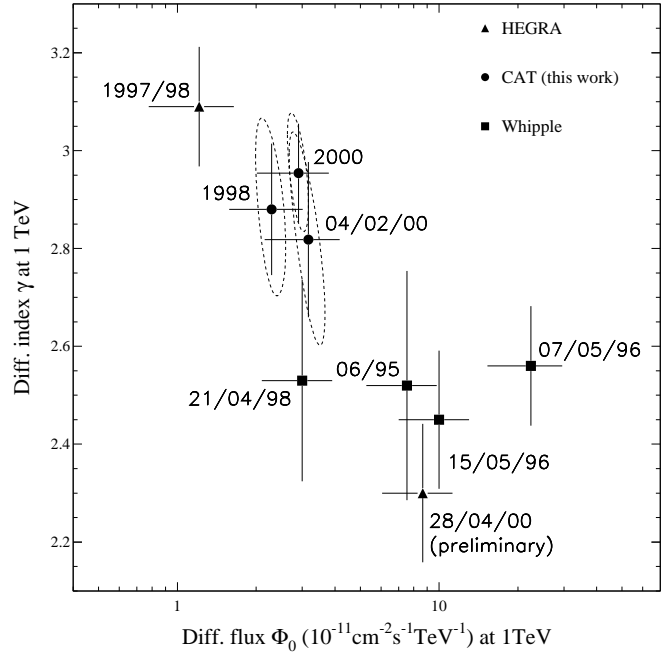


**Fig. 6.** Compilation of spectral measurements on Mkn 421, obtained by the HEGRA (Aharonian et al. 1999; Horns 2001), CAT (this work) and Whipple (Zweerink et al. 1997; Krennrich et al. 1999a, 1999b) experiments between 1995 and 2000. The results are given in the  $\{\phi_0^{\text{pl}}, \gamma^{\text{pl}}\}$  plane of spectral parameters in the power-law hypothesis. While the dashed lines around CAT points show only the 68% confidence level contour (statistical error), the error bars take account, for all measurements, of both statistical and systematic errors, the latter being conservative if unknown:  $(\Delta\phi_0^{\text{pl}}/\phi_0^{\text{pl}})^{\text{syst}} = \pm 30\%$  and  $(\Delta\gamma^{\text{pl}})^{\text{syst}} = \pm 0.10$  were used where these values are not quoted directly. The  $\chi^2$  per d.o.f corresponding to the absence of any dependence of the spectral index with flux is 3.5.

## 4. Discussion

### 4.1. Comparison with other VHE detections

The energy spectrum of Mkn 421 has been measured in the same energy range by the Whipple Observatory (Zweerink et al. 1997; Krennrich et al. 1999a, 1999b) and by the HEGRA experiment (Aharonian et al. 1999; Horns 2001). All these experiments have fitted a power law to the spectrum

and given the values of  $\phi_0^{\text{pl}}$  and of  $\gamma^{\text{pl}}$  in several observation periods corresponding to different levels of activity of the source. Our results for the periods 1998 and 2000 are plotted in Fig. 6 together with their results. This figure includes both statistical *and* systematic errors for *all* measurements. Although CAT data tend to indicate some spectral curvature in 2000, we used the values of  $\gamma^{\text{pl}}$  for this comparison, given that this parameter is in any case clearly indicative of the energy dependence of the spectrum ( $\gamma_0^{\text{cs}} \simeq \gamma^{\text{pl}}$ , see end of Sect. 3.2). In this figure we also added the result obtained during the single night between 4 and 5 February, 2000, for which the high source intensity (see Sect. 3.1) allowed us to extract a spectrum. Since the corresponding errors are larger (see Table 1), this single result is fully compatible with the other two.

Some caution is necessary when comparing results from experiments with different systematic errors. As an example, in the case of a curved spectrum, the value of the energy  $E_0^{\text{cs}}$  (see Table 1) corresponding to the minimal error on the spectral exponent  $\gamma_l^{\text{cs}}$  is not necessarily the same for experiments with different energy thresholds. Possible systematic effects could be responsible for the dispersion of results shown in Fig. 6, since, if one excepts a recent preliminary result from HEGRA (Horns 2001), HEGRA and CAT data favour higher values of  $\gamma^{\text{pl}}$ , whereas data from the Whipple Observatory yield a rather low spectral index. However, experiments showing the largest difference in spectral indices in the figure (Whipple Observatory and HEGRA) are in good agreement on the spectrum of the Crab nebula (Hillas et al. 1998; Aharonian et al. 2000). Furthermore, some evidence for a spectral variability has been already suggested on the basis of the Whipple 1995–96 low-flux data (Zweerink et al. 1997), with a spectral index  $\gamma^{\text{pl}}=2.96\pm0.22$ , but no flux value is quoted in the latter reference, precluding any comparison with the results discussed here.

Data from all experiments with the source in both low and high states would be desirable in order to exclude that experimental effects are responsible for the dispersion seen in Fig. 6. Besides, as different flares may be intrinsically different from each other, the spectral index-flux correlation may not provide us with complete information, thus stressing again the need for more numerous observations.

#### 4.2. Comparison with results on Mkn 501

The second TeV blazar, Mkn 501, underwent a series of intense flares in 1997 observed by all Cherenkov telescopes in the Northern Hemisphere (Djannati-Atai et al. 1999 and references therein). Fig. 7 shows two spectral energy distributions (SEDs) of Mkn 501, as measured by CAT. The first one is the 1997 time-averaged spectrum and the second one corresponds to the single night of April 16<sup>th</sup>, 1997, during which the source reached its highest intensity. The spectral variability observed by CAT on the basis of a hardness ratio (Djannati-Atai et al. 1999) is illustrated here by the shift in the peak energy of the SED: 0.56±0.10 TeV for the average

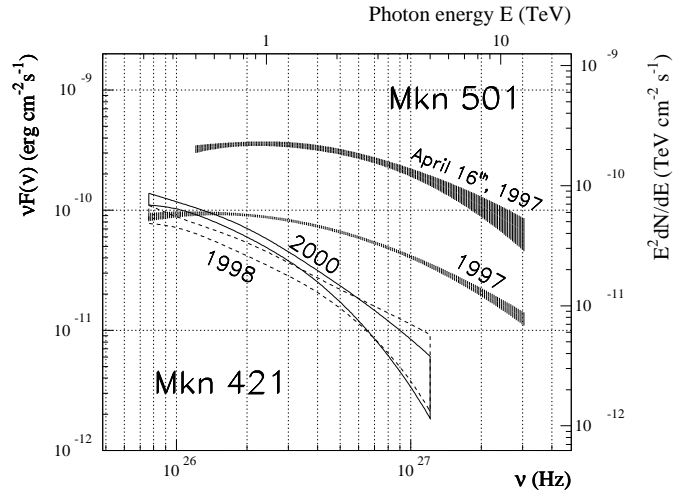


**Fig. 7.** Comparison of the Mkn 421 spectral energy distributions derived in this paper (unfilled areas) with that obtained by CAT for Mkn 501 in 1997 (hatched areas) (Djannati-Atai et al. 1999; Piron 2000). All areas show the 68% confidence level contour given by the likelihood method in the curved shape hypothesis.

spectrum and 0.94±0.16 TeV for the highest flare. Fig. 7 also shows the SEDs of Mkn 421 for the two observation periods 1998 and 2000: both are obtained with the assumption of a curved spectrum (see Sect. 3.2).

In the framework of the phenomenological unification scheme of blazars established by Fossati et al. (1998), the broad-band SED of such a source consists of two components, respectively a low-energy component attributed to synchrotron radiation and a high-energy component peaking in the  $\gamma$ -ray range. Peak energies of the preceding components are correlated and Mkn 501, as observed in 1997, appears to be the most extreme blazar, with the synchrotron part of the SED spectrum peaking in the hard X-ray range and the  $\gamma$ -ray component peaking around or above 500 GeV.

In the case of Mkn 421, the CAT 1998 and 2000 data, and the weakness of its detection by EGRET, when interpreted within the preceding unification scheme, indicate that the peak energy of the high-energy component of the SED lies in the 50 GeV region, while its synchrotron peak is known to lie in the UV-soft X-ray band. A shift of both components towards higher energies during an intense flare, similar to that observed by CAT for Mkn 501 in 1997, would result in a harder spectrum in the energy region covered by Cherenkov telescopes and thus account for the trend shown in Fig. 6. In fact, the spectral hardening of Mkn 421 at TeV energies during flares, if clearly proven, should not be a surprise, since a similar effect has been already observed at a few keV from this source by the ASCA and Beppo-SAX satellites (Takahashi et al. 1999; Malizia et al. 2000), and since X-ray and  $\gamma$ -ray *integrated* emissions of Mkn 421 have proven to be correlated on many occasions (see, e.g., Maraschi et al. 1999;

Takahashi et al. 1999, 2000).

## 5. Conclusions

Along with Mkn 501, Mkn 421 is the most extreme known BL Lac object. The CAT results presented in this paper confirm the high variability of this source at TeV energies, which has been already reported in the past for intense and rapid bursts (Gaidos et al. 1996). Whereas Mkn 501 TeV variability has been observed by CAT from night to night, but never on shorter time-scales, Mkn 421 showed a fast variation in intensity within one hour during the night from 4 to 5 February, 2000. A simple causality argument implies that the  $\gamma$ -ray emitting region must be very compact with a size of  $\sim 10$  light-hours if one takes a typical value of 10 for the geometric Doppler factor (see, e.g., Celotti et al. 1998), which reduces the time-scale in the observer frame.

As for the spectral properties, Mkn 421 has proved to be a little less extreme than Mkn 501. Whereas the latter has shown a  $\gamma$ -ray peak lying above the CAT threshold, Mkn 421 exhibited a power-law spectrum in 1998, indicating that current imaging Cherenkov detectors cover the end part of its spectral energy distribution. However, the 2000 time-averaged spectrum shows some indication of curvature, which in fact has been also marginally observed by the Whipple Observatory at the time of the 1995–96 flaring periods (Krennrich et al. 1999a).

The present observations of Mkn 421 leave some open questions. Firstly, definite conclusions on a possible spectral variability still need simultaneous observations of more numerous flares by different Cherenkov telescopes in order to exclude possible systematic effects between experiments. Secondly, the interpretation of the multi-wavelength spectra of Mkn 421 still suffers from the lack of precise *simultaneous spectral measurements* of the low and high-energy parts of its SED which could bring accurate constraints to models. For instance, in the Synchrotron Self Compton (SSC) model which is often invoked to explain the SED of extreme BL Lac's (Ghisellini et al. 1998), the  $\gamma$ -ray component is interpreted as the result of the inverse Compton process occurring between the ultra-relativistic electrons, which emit synchrotron radiation at low energies, and the latter soft photon field itself. This simple and most natural model predicts a strong correlation between the synchrotron and the  $\gamma$ -ray bump behaviours. Such a correlation has been observed many times on Mkn 421, for example during the coordinated observation campaign in spring 1998, which involved ground-based Cherenkov imaging telescopes (Whipple, HEGRA, and CAT), and the Beppo-SAX and ASCA X-ray satellites (Maraschi et al. 1999; Takahashi et al. 1999, 2000). The correlation was only proven in terms of integrated (and not differential) fluxes due to the lack of statistics. Similarly in 2000, the TeV flaring behaviour of Mkn 421 was accompanied by an overall increase of its keV activity, as for instance continuously recorded by the instruments on board the Rossi X-Ray Timing Explorer satellite (Piron 2000).

SSC models have been already successfully applied to the Beppo-SAX and CAT data obtained on Mkn 501 in 1997 (e.g., Piron 2000; Katarzynski et al. 2001), but alternative scenarios still exist also for this source (e.g., Rachen 1999; Muecke et al. 2001), which consider an  $e^-p$  plasma with synchrotron photons radiated by electrons at low energies and  $\gamma$ -rays emitted at high energies by the products of the proton-induced cascades (from  $\pi^0$  decays and from synchrotron radiation of protons and muons). Thus, in order to address more deeply the crucial problem of the plasma jet content, a richer sample of flares from both blazars, detected at various wavelengths, would be necessary.

*Acknowledgements.* The authors wish to thank the French national institutions IN2P3/CNRS and DAPNIA/DSM/CEA for supporting and funding the CAT project. The CAT telescope was also partly funded by the Languedoc-Roussillon region and the Ecole Polytechnique. The authors also wish to thank Electricité de France for making available to them equipment at the former solar plant “Thémis” and allowing the building of the new telescope and its hangar. They are grateful to the French and Czech ministries of Foreign Affairs for providing grants for physicists’ travel and accommodation expenses. L.R. thanks for the financial support granted by the Ministry of Education of the Czech Republic (Project LN00A006).

## References

- Aharonian, F.A., Akhperjanian, A.G., Andronache, M., et al. 1999, A&A 350, 757
- Aharonian, F.A., Akhperjanian, A.G., Barrio, J.A., et al. 2000, ApJ 539, 317
- Barrau, A., Bazer-Bachi, R., Beyer, E., et al. 1998, NIM A416, 278
- Buckley, J.H., Akerlof, C.W., Biller, S.D., et al. 1996, ApJ 472, L9
- Celotti, A., Fabian, A.C., & Rees, M.J. 1998, MNRAS 293, 239
- Charlot, P., Gabuzda, D., Sol, H., Degrange, B., & Paré, E. 1998, 19<sup>th</sup> Texas Symposium on Relativistic Astrophysics and Cosmology (Paris)
- Djannati-Ataï, A., Piron, F., Barrau, A., et al. 1999, A&A 350, 17
- Fossati, G., Maraschi, L., Celotti, A., Comastri, A., & Ghisellini, G. 1998, MNRAS 299, 433
- Gaidos, J.A., Akerlof, C.W., Biller, S.D., et al. 1996, Nature 383, 319
- Ghisellini, G., Celotti, A., Fossati, G., Maraschi, L., & Comastri, A. 1998, MNRAS 301, 451
- Hartman, R.C., Bertsch, D.L., Bloom, S.D., et al. 1999, ApJSS 123, 79
- Hillas, A.M., Akerlof, C.W., Biller, S.D., et al. 1998, ApJ 503, 744
- Holder, J., for the CELESTE collaboration 2001, High-Energy Gamma-Ray Astronomy (Heidelberg), AIP Conf. Proc. 558, ed. F.A. Aharonian & H.J. Voelk, 635
- Horns, D., for the HEGRA collaboration 2001, 36<sup>th</sup> Rencontres de Moriond on “Very High-Energy Phenomena in the Universe” (Les Arcs), astro-ph/0103514
- Katarzynski, K., Sol, H., & Kus, A. 2001, A&A 367, 809
- Krennrich, F., Akerlof, C.W., Buckley, J.H., et al. 1997, ApJ 481, 758
- Krennrich, F., Biller, S.D., Bond, I.H., et al. 1999a, ApJ 511, 149
- Krennrich, F., Bond, I.H., Bradbury, S.M., et al. 1999b, 26<sup>th</sup> International Cosmic-Ray Conference (Salt-Lake City) 3, 301
- Le Bohec, S., Degrange, B., Punch, M., et al. 1998, NIM A416, 425
- Lin, Y.C., Bertsch, D.L., Chiang, J., et al. 1992, ApJ 401, L61
- Macomb, D.J., Akerlof, C.W., Aller, H.D., et al. 1995, ApJ 449, 99
- Malizia, A., Capalbi, M., Fiore, F., et al. 2000, MNRAS 312, 123 189

Maraschi, L., Fossati, G., Tavecchio, F., et al. 1999, ApJ 526, L81  
 Muecke, A., & Protheroe, R.J. 2001, APh 15, 121  
 Petry, D., Bradbury, S.M., Konopelko, A., et al. 1996, A&A 311, L13  
 Piron, F., for the CAT collaboration 1998, 19<sup>th</sup> Texas Symposium on Relativistic Astrophysics and Cosmology (Paris)  
 Piron, F., for the CAT collaboration 1999a, GeV-TeV Gamma-Ray Astrophysics Workshop (Snowbird), AIP Conf. Proc. 515, ed. B.L. Dingus, M.H. Salamon & D.B. Kieda, 308  
 Piron, F., for the CAT collaboration 1999b, 26<sup>th</sup> International Cosmic-Ray Conference (Salt-Lake City) 3, 326  
 Piron, F. 2000, Ph.D. Thesis, University of Orsay-Paris XI (<http://lpnph2.in2p3.fr/homecat/publi.html>)  
 Punch, M., Akerlof, C.W., Cawley, M.F., et al. 1992, Nature 358, 477  
 Rachen, J.P. 1999, GeV-TeV Gamma-Ray Astrophysics Workshop (Snowbird), AIP Conf. Proc. 515, ed. B.L. Dingus, M.H. Salamon & D.B. Kieda, 41  
 Takahashi, T., Tashiro, M., Madejski, G., et al. 1996, ApJ 470, L89  
 Takahashi, T., Madejski, G., & Kubo, H. 1999, APh 11, 177  
 Takahashi, T., Kataoka, J., Madejski, G., et al. 2000, ApJ 542, L105  
 von Montigny, C., Bertsch, D.L., Chiang, J., et al. 1995, ApJ 440, 525  
 Zwaarink, J.A., Akerlof, C.W., Biller, S.D., et al. 1997, ApJ 490, L141

## Appendix A: Spectra and light curve extraction

### A.1. The spectral analysis procedure

Here we give the expression of the likelihood function  $\mathcal{L}$  used for spectral reconstruction, using the same notations as in Sect. 2.3. We start with an assumption on the spectral shape by choosing a given law  $\left(\frac{d\phi}{dE}\right)^{\text{pred}}$ , which includes the set  $\{\Lambda\}$  of parameters to fit. Then, for each 2D-bin  $\Delta_{i_z, i_e}$ , corresponding to the zenith angle interval  $[\theta_{i_z}^{\min}, \theta_{i_z}^{\max}]$  and to the estimated energy interval  $[\tilde{E}_{i_e}^{\min}, \tilde{E}_{i_e}^{\max}]$ , let us define:

- $n_{i_z, i_e}$  and  $p_{i_z, i_e}$  as the numbers of events passing the selection cuts in the ON and OFF data, respectively;
- $\beta_{i_z}$  as the normalisation factor between ON and OFF observations, obtained from the contents of the respective  $\alpha$  distributions in the range from  $20^\circ$  to  $120^\circ$  (the control region) (see Fig. 1);
- $S_{i_z, i_e} = n_{i_z, i_e} - \beta_{i_z} p_{i_z, i_e}$  as the observed number of  $\gamma$ -ray events, and  $\delta S_{i_z, i_e} = \sqrt{n_{i_z, i_e} + \beta_{i_z}^2 p_{i_z, i_e}}$  as its error;
- $S_{i_z, i_e}^{\text{pred}}$  as the predicted number of  $\gamma$ -ray events: if we note  $\Upsilon(\theta_z, E_\gamma \rightarrow \tilde{E}_\gamma) d\tilde{E}_\gamma$  for the probability, at fixed zenith angle  $\theta_z$  and *real* energy  $E_\gamma$ , to get an *estimated* energy  $\tilde{E}_\gamma$  within the interval  $[\tilde{E}_\gamma, \tilde{E}_\gamma + d\tilde{E}_\gamma]$ , then

$$S_{i_z, i_e}^{\text{pred}} = T_{\text{ON}} \int_{\tilde{E}_{i_e}^{\min}}^{\tilde{E}_{i_e}^{\max}} d\tilde{E} \int_0^\infty dE \left(\frac{d\phi}{dE}\right)^{\text{pred}} \times \mathcal{A}_{\text{eff}}(\overline{\theta_{i_z}}, E) \Upsilon(\overline{\theta_{i_z}}, E \rightarrow \tilde{E}), \quad (\text{A.1})$$

where  $T_{\text{ON}}$  is the total ON-source time of observation,  $\mathcal{A}_{\text{eff}}$  is the effective detection area, and where  $\overline{\theta_{i_z}}$  is defined by  $\cos(\overline{\theta_{i_z}}) \equiv \frac{1}{2} [\cos(\theta_{i_z}^{\min}) + \cos(\theta_{i_z}^{\max})]$ ;

- $\overline{p_{i_z, i_e}}$  the mean predicted number of events in the OFF data;
- $\overline{n_{i_z, i_e}} = S_{i_z, i_e}^{\text{pred}} + \beta_{i_z} \overline{p_{i_z, i_e}}$  the mean predicted number of events in the ON data.

The observed numbers  $n_{i_z, i_e}$  and  $p_{i_z, i_e}$  have Poissonian probability distributions  $\mathcal{P}(n_{i_z, i_e})$  and  $\mathcal{P}(p_{i_z, i_e})$ , respectively, and the likelihood function is as follows:

$$\mathcal{L}(\{\Lambda\}, \{\overline{p_{i_z, i_e}}\}) = \prod_{i_z, i_e} \mathcal{P}(n_{i_z, i_e}) \mathcal{P}(p_{i_z, i_e}). \quad (\text{A.2})$$

The quantities  $\overline{p_{i_z, i_e}}$ , which are unknown, can be determined by maximizing the function  $\mathcal{L}$ : the relations  $\frac{\partial \log(\mathcal{L})}{\partial \overline{p_{i_z, i_e}}} \equiv 0$  lead to the solutions  $\overline{p_{i_z, i_e}} = \frac{1}{2\beta_{i_z}(\beta_{i_z} + 1)} \left[ a_{i_z, i_e} + \sqrt{a_{i_z, i_e}^2 + 4\beta_{i_z}(\beta_{i_z} + 1)p_{i_z, i_e} S_{i_z, i_e}^{\text{pred}}} \right]$ , with  $a_{i_z, i_e} = \beta_{i_z}(n_{i_z, i_e} + p_{i_z, i_e}) - (\beta_{i_z} + 1)S_{i_z, i_e}^{\text{pred}}$ .

Finally, we reinject these expressions in Eq. (A.2), eliminate the “constant” terms which only depend on  $n_{i_z, i_e}$  or  $p_{i_z, i_e}$ , and get:

$$\log [\mathcal{L}(\{\Lambda\})] = \sum_{i_z, i_e} \left[ n_{i_z, i_e} \log \left( S_{i_z, i_e}^{\text{pred}} + \beta_{i_z} \overline{p_{i_z, i_e}} \right) + p_{i_z, i_e} \log (\overline{p_{i_z, i_e}}) - (\beta_{i_z} + 1) \overline{p_{i_z, i_e}} - S_{i_z, i_e}^{\text{pred}} \right]. \quad (\text{A.3})$$

The  $\{\Lambda\}$  parameters, included in this expression through Eq. (A.1), are the only unknown quantities left: their values are determined using an iterative procedure of maximization, which leads to the final fitted values and their covariance matrix  $V$ .

### A.2. Integral flux determination

When computing an integral flux, one must again take care of the telescope detection threshold increase with zenith angle  $\theta_z$ ; thus, let us denote:

- $\tilde{E}^{\text{int}}[\theta_z]$  for the unique energy which verifies  $\mathcal{A}_{\text{eff}}(\theta_z, \tilde{E}^{\text{int}}) \equiv \mathcal{A}_{\text{eff}}(0^\circ, 250 \text{ GeV})$ ;
- $S^{\text{int}}$  for the total number of  $\gamma$ -ray events observed within the selection cuts with an *estimated* energy above  $\tilde{E}^{\text{int}}[\theta_z]$  ( $S^{\text{int}}$  is determined by a simple “ON–OFF” subtraction), and  $\delta S^{\text{int}}$  for its error.

To convert  $S^{\text{int}}$  into the corresponding integral flux  $\Phi$  above 250 GeV, we use the following proportionality relation:

$$\Phi = \frac{S^{\text{int}}}{S^{\text{int, best}}} \times \int_{250 \text{ GeV}}^\infty \left(\frac{d\phi}{dE}\right)^{\text{best}} dE,$$

where  $\left(\frac{d\phi}{dE}\right)^{\text{best}}$  is the source differential spectrum measured as explained in Sect. 2.3, and  $S^{\text{int, best}}$  is the number of  $\gamma$ -ray events predicted from this law above  $\tilde{E}^{\text{int}}[\theta_z]$ :

$$S^{\text{int, best}} = T_{\text{ON}} \int_{\tilde{E}^{\text{int}}[\theta_z]}^\infty d\tilde{E} \int_0^\infty dE \left(\frac{d\phi}{dE}\right)^{\text{best}} \times \mathcal{A}_{\text{eff}}(\theta_z, E) \Upsilon(\theta_z, E \rightarrow \tilde{E}).$$

Finally, the error on  $\Phi$  is simply estimated as  $\delta\Phi = \frac{\delta S^{\text{int}}}{S^{\text{int}}} \times \Phi$ .

**Table B.1.** Mkn 421 available statistics.

$\Delta_{i_e}$	1998					2000 (except 4–5/02)					4–5/02/2000				
	$T_{\text{ON}}=6.2 \text{ h}$		$\theta_z \in [0^\circ; 28^\circ]$			$T_{\text{ON}}=8.4 \text{ h}$		$\theta_z \in [0^\circ; 28^\circ]$			$T_{\text{ON}}=3.5 \text{ h}$		$\theta_z \in [0^\circ; 28^\circ]$		
	$T_{\text{OFF}}=9.5 \text{ h}$	$S_\gamma=735 \pm 57$	$T_{\text{OFF}}=16.7 \text{ h}$	$S_\gamma=1424 \pm 71$	$T_{\text{OFF}}=17.6 \text{ h}$	$S_\gamma=609 \pm 40$	$n_{i_e}$	$p_{i_e}$	$S_{i_e}$	$\delta S_{i_e}$	$N_{\sigma i_e}$	$n_{i_e}$	$p_{i_e}$	$S_{i_e}$	$\delta S_{i_e}$
0.3–0.5	615	445	170	29	5.8	1351	993	358	44	8.2	464	318	146	23	6.4
0.5–0.8	790	536	254	35	7.3	1267	731	536	41	13.1	561	300	261	25	10.4
0.8–1.3	452	301	151	26	5.7	690	411	279	30	9.2	300	172	128	18	7.0
1.3–2.0	229	123	107	18	5.9	335	158	175	21	8.6	138	64	74	12	6.0
2.0–5.0	119	66	53	13	4.0	165	89	76	15	5.1	–	–	–	–	–

**Table B.2.** Covariance matrices elements of Mkn 421 spectra.

Period	$V_{\phi\phi}^{\text{pl}}$	$V_{\phi\gamma}^{\text{pl}}$	$V_{\gamma\gamma}^{\text{pl}}$	$V_{\phi\phi}^{\text{cs}}$	$V_{\phi\gamma}^{\text{cs}}$	$V_{\phi\beta}^{\text{cs}}$	$V_{\gamma\gamma}^{\text{cs}}$	$V_{\gamma\beta}^{\text{cs}}$	$V_{\beta\beta}^{\text{cs}}$
1998	$3.97 \times 10^{-2}$	$-1.24 \times 10^{-2}$	$1.44 \times 10^{-2}$	$1.03 \times 10^{-1}$	$-1.10 \times 10^{-2}$	$1.13 \times 10^{-1}$	$2.35 \times 10^{-2}$	$3.28 \times 10^{-2}$	$2.35 \times 10^{-1}$
2000	$3.19 \times 10^{-2}$	$-8.65 \times 10^{-3}$	$6.51 \times 10^{-3}$	$7.80 \times 10^{-2}$	$-8.36 \times 10^{-4}$	$6.45 \times 10^{-2}$	$1.68 \times 10^{-2}$	$2.91 \times 10^{-2}$	$1.36 \times 10^{-1}$
4–5/02/2000	$1.12 \times 10^{-1}$	$-3.84 \times 10^{-2}$	$2.16 \times 10^{-2}$	$1.38 \times 10^{-1}$	$-3.45 \times 10^{-2}$	$3.63 \times 10^{-2}$	$1.53 \times 10^{-1}$	$2.86 \times 10^{-1}$	$6.57 \times 10^{-1}$

## Appendix B: More on Mkn 421 spectra

### B.1. Available statistics

The statistics used for extracting the Mkn 421 spectra are given in Table B.1. With the same notations used in this paper, we write:

- the data zenith angle amplitude, and the ON and OFF-source observation durations,  $T_{\text{ON}}$  and  $T_{\text{OFF}}$ ;
- for each of the  $n_e$  energy intervals  $\Delta_{i_e} \equiv [\tilde{E}_{i_e}^{\text{min}}, \tilde{E}_{i_e}^{\text{max}}]$  (in TeV):
  - the numbers of events passing the selection cuts in the ON and OFF data,
  - $n_{i_e} = \sum_{i_z} n_{i_z, i_e}$  and  $p_{i_e} = \sum_{i_z} \beta_{i_z} p_{i_z, i_e}$ ;
  - the observed number of  $\gamma$  events,  $S_{i_e} = n_{i_e} - p_{i_e}$ , and its error,  $\delta S_{i_e} = (\sum_{i_z} n_{i_z, i_e} + \beta_{i_z}^2 p_{i_z, i_e})^{1/2}$ ;
  - the statistical significance  $N_{\sigma i_e} = S_{i_e} / \delta S_{i_e}$ ;
- the observed total number of  $\gamma$  events,  $S_\gamma = \sum_{i_e} S_{i_e}$ , and its error,  $\delta S_\gamma = (\sum_{i_e} \delta S_{i_e}^2)^{1/2}$ .

### B.2. Covariance matrices

Let  $V^{\text{pl}}$  and  $V^{\text{cs}}$  be the two covariance matrices of spectral parameters for the  $\mathcal{H}^{\text{pl}}$  and  $\mathcal{H}^{\text{cs}}$  hypotheses (see Sect. 2.3), respectively:

$$V^{\text{pl}} = \begin{pmatrix} V_{\phi\phi}^{\text{pl}} & V_{\phi\gamma}^{\text{pl}} \\ V_{\phi\gamma}^{\text{pl}} & V_{\gamma\gamma}^{\text{pl}} \end{pmatrix} \text{ and } V^{\text{cs}} = \begin{pmatrix} V_{\phi\phi}^{\text{cs}} & V_{\phi\gamma}^{\text{cs}} & V_{\phi\beta}^{\text{cs}} \\ V_{\phi\gamma}^{\text{cs}} & V_{\gamma\gamma}^{\text{cs}} & V_{\gamma\beta}^{\text{cs}} \\ V_{\phi\beta}^{\text{cs}} & V_{\gamma\beta}^{\text{cs}} & V_{\beta\beta}^{\text{cs}} \end{pmatrix}.$$

The values of these matrices elements are given in Table B.2 for each spectrum of Mkn 421 obtained in this paper.

In the power-law hypothesis, the energy  $E_d$  at which the values of  $\phi_0^{\text{pl}}$  et  $\gamma^{\text{pl}}$  are decorrelated writes:

$$E_d = \exp \left[ \frac{V_{\phi\gamma}^{\text{pl}}}{\phi_0^{\text{pl}} V_{\gamma\gamma}^{\text{pl}}} \right] \text{ TeV.}$$

At this decorrelation energy, the width of the hatched area representing the 68% confidence level contour, is minimum: for instance, we find  $E_d=690$  GeV for the 1998 time-averaged spectrum of Mkn 421 shown in Sect. 3.2.

In the curved shape hypothesis, the energy-dependent exponent  $\gamma_l^{\text{cs}}(E_{\text{TeV}}) = \gamma^{\text{cs}} + \beta^{\text{cs}} \log_{10} E_{\text{TeV}}$  has a minimal error at the energy  $E_0^{\text{cs}} = 10^{\frac{-V_{\gamma\beta}^{\text{cs}}}{V_{\beta\beta}^{\text{cs}}}}$  TeV; the corresponding value of  $\gamma_l^{\text{cs}}$  writes

$$\gamma_0^{\text{cs}} \equiv \gamma_l^{\text{cs}}(E_0^{\text{cs}}) = \gamma^{\text{cs}} - \beta^{\text{cs}} \frac{V_{\gamma\beta}^{\text{cs}}}{V_{\beta\beta}^{\text{cs}}},$$

and its error

$$\delta \gamma_0^{\text{cs}} \equiv \delta \gamma_l^{\text{cs}}(E_0^{\text{cs}}) = \sqrt{V_{\gamma\gamma}^{\text{cs}} - \frac{V_{\gamma\beta}^{\text{cs}}}{V_{\beta\beta}^{\text{cs}}}}.$$